

Velocity-resolved Reverberation Mapping of Changing-look Active Galactic Nucleus NGC 4151 During Outburst Stage: Evidence for Kinematics Evolution of Broad-line Region

SHA-SHA LI,^{1,2} HAI-CHENG FENG,^{1,2,3} H. T. LIU,^{1,2,4} J. M. BAI,^{1,2,4} RUI LI,³ KAI-XING LU,^{1,2,4} JIAN-GUO WANG,^{1,2,4} YING-KE HUANG,^{5,6} AND ZHI-XIANG ZHANG⁷

¹*Yunnan Observatories, Chinese Academy of Sciences, Kunming, 650011, Yunnan, People's Republic of China*

²*Key Laboratory for the Structure and Evolution of Celestial Objects, Chinese Academy of Sciences, Kunming 650011, Yunnan, People's Republic of China*

³*University of Chinese Academy of Sciences, Beijing 100049, People's Republic of China*

⁴*Center for Astronomical Mega-Science, Chinese Academy of Sciences, 20A Datun Road, Chaoyang District, Beijing 100012, People's Republic of China*

⁵*Qian Xuesen Laboratory of Space Technology, China Academy of Space Technology, 104 Youyi Road, Haidian District, Beijing, 100094, People's Republic of China*

⁶*Multi-disciplinary Research Division, Institute of High Energy Physics, Chinese Academy of Sciences, 19B Yuquan Road, Beijing 100049, People's Republic of China*

⁷*Department of Astronomy, Xiamen University, Xiamen, Fujian 361005, People's Republic of China*

ABSTRACT

Changing-look active galactic nucleus NGC 4151, which has attracted a lot of attention, is undergoing the second dramatic outburst stage in its evolutionary history. To investigate the geometry and kinematics of the broad-line region (BLR), and measure the mass of supermassive black hole in NGC 4151, we perform a seven-month photometric and spectroscopic monitoring program in 2020–2021, using the 2.4 m telescope at Lijiang Observatory. We successfully measure the time lags of the responses from broad H α , H β , H γ , He I, and He II emission lines to continuum variation, which are $7.63^{+1.85}_{-2.62}$, $6.21^{+1.41}_{-1.13}$, $5.67^{+1.65}_{-1.94}$, $1.59^{+0.86}_{-1.11}$, and $0.46^{+1.22}_{-1.06}$ days, respectively, following radial stratification. The ratios of time lags among these lines are 1.23 : 1.00 : 0.91 : 0.26 : 0.07. We find that the continuum lag between the ultraviolet and optical bands can significantly affect the lag measurements of He I and He II. Virial and infalling gas motions coexist in this campaign, which is different from previous results, implying the evolutionary kinematics of BLR. Based on our measurements and previous ones in the literature, we confirm that the BLR of NGC 4151 is basically virialized. Finally, we compute the black hole mass through multiple lines, and the measurement from H β to be $3.94^{+0.90}_{-0.72} \times 10^7 M_{\odot}$, which is consistent with previous results. The corresponding accretion rate is $0.02^{+0.01}_{-0.01} L_{\text{Edd}} c^{-2}$, implying a sub-Eddington accretor.

Keywords: Active galactic nuclei (16), Seyfert galaxies (1447), Time domain astronomy (2109), Reverberation mapping (2019), Supermassive black holes (1663)

1. INTRODUCTION

Broad emission lines, one of the most prominent features in active galactic nuclei (AGNs), are emitted from the broad-line region (BLR). The BLR is one of the main components in the interior part of AGNs located between the accretion disk and dust structure (Antonucci 1993). It is generally believed that motions of BLR clouds are dominated by gravity of central supermassive black hole (SMBH), while some researchers argued that the radiation pressure from the accretion disk can also contribute to non-negligible effects. Although broad emission lines allow to study the geometry and kinematics of the BLR, and measure the mass of SMBH, the

BLR is still not yet fully understood. The BLR is too small to be directly spatial resolved by most telescopes. To date, only three AGNs have been resolved using the infrared interferometry (e.g., Gravity Collaboration et al. 2018), therefore, other approaches are urgently needed.

Among them, reverberation mapping (RM) is an effective way of investigating the BLR and SMBH, which subtly uses the time resolution of the telescope to substitute the spatial resolution (e.g., Blandford & McKee 1982; Cackett et al. 2021). In principle, the continuum radiated from the accretion disk acts as ionizing photons to ionize the gas of the BLR, and this photoionization process generates the emission lines that are broadened by the BLR cloud motion into the corresponding broad emission lines. The characteristic size of the BLR can be inferred from monitoring the responses of broad emission lines to continuum variations and measuring the time delays between broad emission-line and

continuum light curves. When combining the size of the BLR with broad emission-line velocity, and using the virial relationship, one can estimate the mass of SMBH. Over the past four decades, the RM method has measured the black hole masses of ~ 100 AGNs, and has become a standard tool for measuring the masses of SMBHs in AGNs (e.g., Kaspi et al. 2000; Peterson et al. 2004; Bentz et al. 2009; Barth et al. 2013; Du et al. 2014; Fausnaugh et al. 2017; De Rosa et al. 2018; Lu et al. 2019; Zhang et al. 2019; Hu et al. 2021; Bao et al. 2022). Additionally, the application of RM to the accretion disk and torus can measure the size of disk (e.g., Edelson et al. 2017; Cackett et al. 2020; Fian et al. 2022), and determine dust sublimation radius (e.g., Koshida et al. 2014; Oknyansky et al. 2014; Lyu & Rieke 2021; Lyu et al. 2022).

Here, the geometry and kinematics of BLR can be inferred from velocity-resolved RM analysis utilizing high-quality spectral data. The details are derived by measuring time lag as a function of line-of-sight velocity for the broad emission line. Currently, more than 30 AGNs have been measured using this method, and different kinematic characteristics of their BLR, such as rotation, inflow, and outflow, have been obtained (e.g., Du et al. 2016; Williams et al. 2018; Brotherton et al. 2020; Horne et al. 2021; Lu et al. 2021; U et al. 2022; Villafaña et al. 2022). And a few well-studied AGNs were measured multiple times for velocity-resolved results in different periods. For example, Xiao et al. (2018) recovered velocity-delay maps of NGC 5548 from multi-year data and found that the kinematics of the BLR varied between inflow and virial. Then, Hu et al. (2020) detected that the kinematics of the BLR in PG 2130+099 changed from virialized motion to inflow, and the timescale of change was less than one year. However, some other AGNs, e.g., NGC 3516, showed nearly consistent velocity-resolved signature over a decade (Denney et al. 2010; Feng et al. 2021a), indicating the complicated evolution in BLR. Therefore, to investigate the kinematic evolution of BLR, multiple velocity-resolved time delay measurements are necessary.

To achieve the above-mentioned purpose of studying the kinematic evolution of BLR, NGC 4151 is selected for RM monitoring in this work. As one of the brightest ($m_V = 11.48$ mag), nearest ($z = 0.003326$), and earliest Seyfert galaxies to be discovered (Seyfert 1943), NGC 4151 was one of the best-studied AGNs. This target has been monitored by multiple RM projects in the last three decades including optical RM campaigns (Maoz et al. 1991; Kaspi et al. 1996; Peterson et al. 2004; Bentz et al. 2006; De Rosa et al. 2018; Bentz et al. 2022), and ultraviolet (UV) RM campaigns (Clavel et al. 1990; Ulrich & Horne 1996; Metzroth et al. 2006). Among these projects, Ulrich & Horne (1996), De Rosa et al. (2018) and Bentz et al. (2022) also presented velocity-delay maps of BLR in the UV and optical emission lines, respectively. And these results provide a suitable condition for investigating the kinematic evolution of BLR. Furthermore, NGC 4151 is one of the few AGNs with accretion disk RM (Edelson et al. 1996, 2017), which limits the size and structure of the disk. Also, it is a changing-look

(CL) AGN which usually shows large variability amplitudes in both continuum and emission lines. In the past, NGC 4151 repeated CL phenomenon. For example, in 1984 the spectral type of NGC 4151 changed from type 1 to type 2 (Penston & Perez 1984), and Shapovalova et al. (2008) found a change from type 1.5 to type 1.8 between 1996 and 2006. Historical data of NGC 4151 show an extreme outburst lasting for more than ten years, and it recently arrived at the second outburst stage. Such unusual variability of continuum should lead to dramatic changes in the radiation pressure on BLR, and then in the properties of geometry and kinematics of BLR, which provide a good opportunity to investigate the nature of BLR during this period. NGC 4151 is only one of two AGNs with several methods for measuring black hole mass (the other is NGC 3227), including gas dynamical modeling (Hicks & Malkan 2008), and stellar dynamical modeling (Onken et al. 2014; Roberts et al. 2021). Thus, NGC 4151 is an ideal candidate to verify the reliability of RM measurement when compared to other results.

In this work, we report the results from the RM campaign of NGC 4151. We successfully measure time lags of broad $H\alpha$, $H\beta$, $H\gamma$, He I, and He II emission lines, and obtain their velocity-resolved maps, respectively. In comparison with previous velocity-delay maps, the BLR kinematics of NGC 4151 changed, implying evolutionary kinematics of BLR. Furthermore, we also calculate the black hole mass and dimensionless accretion rate of NGC 4151, and the result indicates a sub-accretor. This paper is arranged as follows. Observations and data reduction are introduced in Section 2. Section 3 presents light-curve measurements, variability characteristics, and intercalibration of multi-band continuum light curves. Time lag analysis, and measurements of black hole mass and dimensionless accretion rate are given in Section 4. In Section 5, we discuss the long-term variability trend, kinematics characteristics of BLR, and comparison with previous results in measurements of time lag and black hole mass. Section 6 provides a brief summary.

Throughout the paper, we adopt the distance to NGC 4151 of 15.8 Mpc (Yuan et al. 2020).

2. OBSERVATIONS AND DATA REDUCTION

NGC 4151 was monitored between 2020 November and 2021 June using the 2.4 m telescope of Lijiang Observatory, Yunnan Observatories, Chinese Academy of Sciences. The telescope is located at $100^{\circ}01'48''$ east longitude and $26^{\circ}41'42''$ north latitude. This Observatory can be divided into the dry season and rainy season. The rainy season is from July to September with few sunny days, while the rest of the year is the dry season. The weather during the dry season is clear, so we can perform RM observations. Additionally, the telescope is equipped with Yunnan Faint Object Spectrograph and Camera (YFSOC) which can quickly switch observing modes and is convenient. Thus, we carried out photometric and spectroscopic observations each night. The detailed information about the telescope and Observatory were described in Wang et al. (2019) and Xin et al. (2020), respectively.

2.1. Photometry

Before or after spectroscopic observations, we would use the Johnson B filter and take 30 s exposure to get the broadband image. There are two motivations for performing photometry. Firstly, the photometric data is available for inspecting our spectral data quality. Secondly, we can examine whether the comparison star is unchanging (Hu et al. 2020a). The data was reduced by the standard IRAF procedures, including bias subtraction and flat-fielding correction. Since the field of view (FoV) is about $10' \times 10'$, we could select several stars in the FoV for differential photometry. In addition, we employed a circular aperture with a radius of $4''.24$ (corresponding to 15 pixels), and the inner and outer radii of the background annulus are $14''.15$ and $19''.81$ (corresponding to 50 and 70 pixels), respectively. The size of the aperture was estimated based on the FWHM of stars. Finally, we successfully obtained 55 epochs of photometric observations, and Figure 1 shows the light curves of our target and comparison star. The standard deviation of the light curve of the comparison star is ~ 0.017 mag, suggesting that it was stable and can be used to calibrate spectral flux.

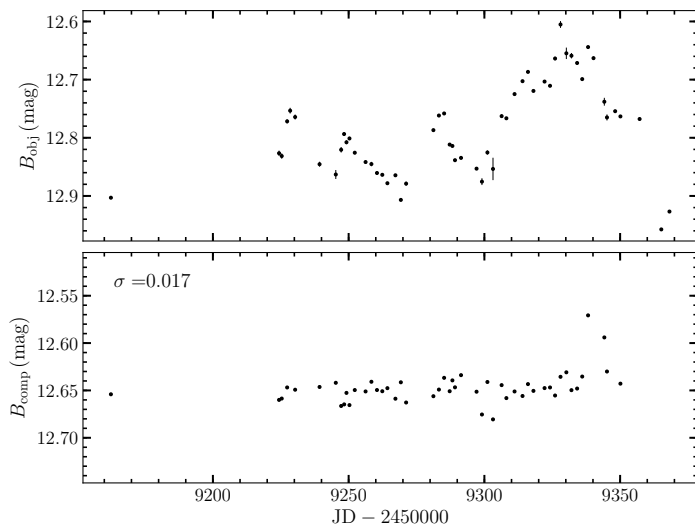


Figure 1. The photometric light curves of Johnson B filter of NGC 4151 (upper) and comparison star (lower).

2.2. Spectroscopy

For spectroscopic observations, we applied a slit of $2''.5$ width to mitigate light loss after taking into account the local average seeing $\sim 1''.5$. The telescope provides various grisms with different resolutions, and we chose Grism 3 possessing a dispersion of $2.86 \text{ \AA pixel}^{-1}$. Besides that, we also added a UV-blocking filter in observation which can cut off wavelength less than 4150 \AA , accordingly eliminating secondary spectral contamination (Feng et al. 2021a,b). Indeed, taking advantage of the long-slit spectra of the Lijiang 2.4 m telescope, we can simultaneously put NGC 4151 and the comparison star into the slit to adjust the flux of spectroscopy (Maoz

et al. 1990; Kaspi et al. 2000). We spent 600 s exposure on each spectrum and utilized IRAF software to process spectra. Furthermore, the extraction aperture and background cover the same region as photometry.

Concerning the flux calibration, we adopted the following steps. First, we picked some spectra of the standard star observed on clear nights to measure the absolute flux of the comparison star. Second, we combined the flux calibrated spectra of the comparison star to generate a template spectrum. Finally, we compared the individual spectrum of the comparison star with the template spectrum to create a response function, which was used for NGC 4151 spectral calibration. As above-mentioned (Section 2.1), the comparison star is invariable and can be employed for calibration. At last, we obtained 41 epochs spectra, one of which was taken using $5''.05$ width slit. The spectral average signal-to-noise ratio at the rest-frame 5100 \AA is $\sim 149 \text{ pixel}^{-1}$.

2.3. Other Telescopes

Nowadays, with the development of time-domain survey projects, such as the All-Sky Automated Survey for Supernovae (ASAS-SN¹) and the Zwicky Transient Facility (ZTF²), it is convenient to increase the cadence and length of observation or to explore the long-term variability. ASAS-SN is used to image the whole sky, and the current depth can reach 18 mag. It consists of multiple stations, and provides 3 dithered 90 s exposures in V or g bands (Shappee et al. 2014; Kochanek et al. 2017). Aperture photometry is applied to handle the images with an aperture radius of $16''.0$.

ZTF is another survey using a 48-inch telescope at Palomar observatory with 47 deg^2 FoV to monitor transients and variable astronomy phenomenons (Bellm et al. 2019; Graham et al. 2019; Masci et al. 2019). It scans the Northern Sky on a three-day cadence and the Galactic Plane every night. The depths of g and r bands in 30 s exposures are 20.8 and 20.6 mag, respectively. In addition, the image quality for g and r are $2''.1$ and $2''.0$, respectively. But in this work, we adopt the Automatic Learning for the Rapid Classification of Events (ALeRCE³) API to get accurate ZTF data. ALeRCE has succeeded in managing the ZTF alert stream before it is developed for the Legacy Survey of Space and Time (Förster et al. 2021; Sánchez-Sáez et al. 2021).

3. MEASUREMENTS

3.1. Light Curves

There are two methods to measure light curves of emission lines, one of which is integration and the other is spectral decomposition. For the integration method, we should first select two continuum windows on either side of the emis-

¹ <http://www.astronomy.ohio-state.edu/asassn/index.shtml>

² <https://www.ztf.caltech.edu/>

³ <https://alerce.online>

Table 1. The Broad Emission-line and Photometric Light Curves

Spectra						Photometry		
JD - 2,450,000	$F_{H\alpha}$	$F_{H\beta}$	$F_{H\gamma}$	$F_{He I}$	$F_{He II}$	JD - 2,450,000	mag	Obs
9162.44	147.136 ± 1.821	46.207 ± 0.725	19.227 ± 0.626	7.533 ± 0.216	8.290 ± 1.395	9153.05	12.959 ± 0.020	ZTF
9224.38	163.628 ± 1.828	51.484 ± 0.735	22.135 ± 0.652	8.387 ± 0.244	13.503 ± 1.400	9156.02	12.959 ± 0.020	ZTF
9225.37	164.933 ± 1.826	52.237 ± 0.732	21.685 ± 0.641	8.742 ± 0.236	14.133 ± 1.399	9158.02	12.924 ± 0.019	ZTF
9230.31	167.195 ± 1.830	53.336 ± 0.738	23.489 ± 0.661	8.966 ± 0.255	14.731 ± 1.402	9162.43	12.903 ± 0.017	LJ
9239.30	169.726 ± 1.833	52.926 ± 0.742	22.769 ± 0.671	9.259 ± 0.265	13.153 ± 1.404	9166.01	12.867 ± 0.019	ZTF

NOTE—The emission-line flux is in units of $10^{-13} \text{ erg s}^{-1} \text{ cm}^{-2}$. The photometry includes the B band data of Lijiang and the g band data of ZTF, which are intercalibrated by PyCALI, and are also marked with the specific telescope in the “Obs” column, “LJ” refers to Lijiang 2.4 m telescope, and “ZTF” refers to ZTF. (This table is available in its entirety in a machine-readable form in the online journal.)

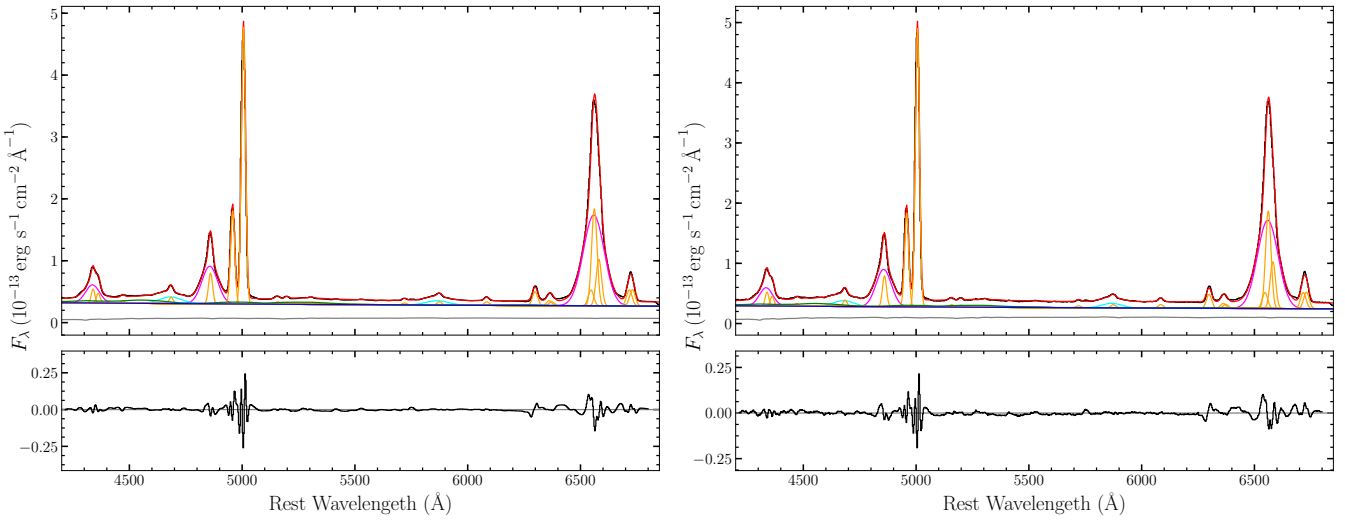


Figure 2. The upper left panel shows the fit of the mean spectrum, where the broad Balmer lines ($H\alpha$, $H\beta$, $H\gamma$) are shown in magenta, the broad He I and He II are shown in cyan, and orange lines represent narrow emission lines. The blue, green, and grey lines correspond to AGN power-law, Fe II template, and host galaxy template, respectively. Additionally, the red line symbolizes the best-fit model, and the original spectrum is shown in black. The lower left panel is fitting residuals. The right panels are the same as the left panels but for an individual spectrum.

sion line and fit them with a straight line as the underlying continuum contribution. Then, the continuum is subtracted from the emission-line profile, and the continuum-subtraction emission-line profile is integrated as emission-line flux. This method is common to extract emission-line flux in RM (e.g., Kaspi et al. 2000; Peterson et al. 2004; Bentz et al. 2009; Hu et al. 2021), but is not suited for mixed and weak emission lines like He II and Fe II. Alternatively, the spectral decomposition can mitigate the contamination of other contributions, because it can decompose pure emission-line components to obtain multi-line light curves (e.g., Barth et al. 2015; Hu et al. 2015; Li et al. 2021). Here, we adopt multi-component spectral fitting to calculate emission-line light curves, and introduce the fitting scheme in the following.

Before the fitting, the galactic extinction and redshift need to be corrected. According to the dust map of Schlafly &

Finkbeiner (2011), the value of $A_V = 0.074$ mag is provided by NED⁴. We adopted an extinction law of $R_V = 3.1$ to fix reddening (Cardelli et al. 1989; O’Donnell 1994). Then, each spectrum was shifted to the rest-frame using the $[O III]\lambda 5007$. After these corrections, we decomposed the spectra using DASpec⁵ software with a GUI interface based on the Levenberg-Marquardt technique. We use all spectra except one with slit $5''05$ to produce a mean spectrum and fit it at first. The detailed fitting strategy involves several aspects: (1) the host galaxy template from Bruzual & Charlot (2003); (2) a Fe II template from Boroson & Green (1992); (3) a power-law representing AGN continuum; (4) a single-Gaussian function is used to describe each of the

⁴ <http://ned.ipac.caltech.edu>

⁵ <https://github.com/PuDu-Astro/DASpec>

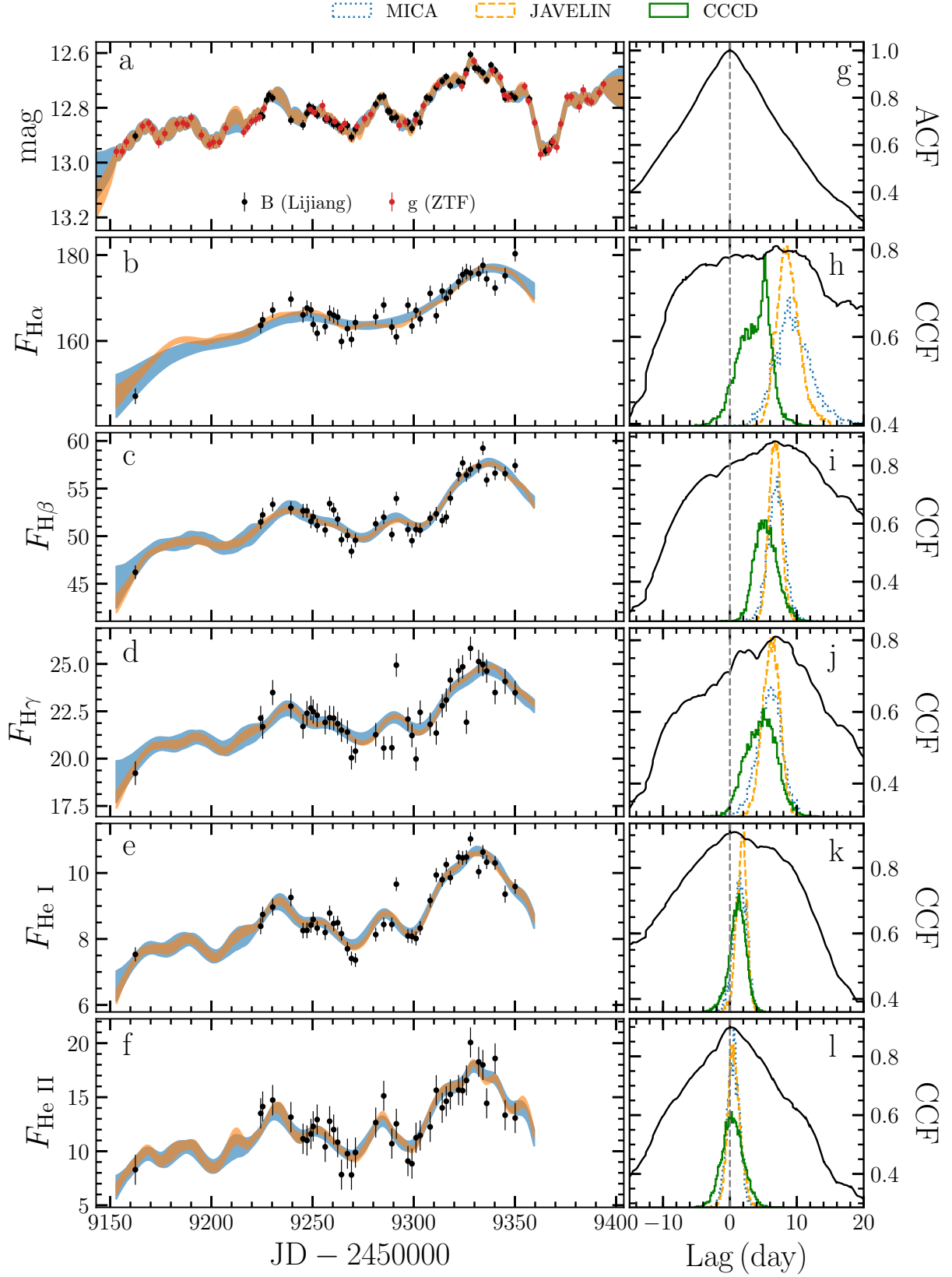


Figure 3. The left panels show photometry, $H\alpha$, $H\beta$, $H\gamma$, He I, and He II light curves. Panel (a) is the intercalibrated result of B (Lijiang) and g (ZTF). The blue and orange shaded regions represent light curves reconstructed by MICA and JAVELIN. The right panels show time-lag distributions. Panel (g) shows the photometric autocorrelation function (ACF). Furthermore, in panels (h)-(l), the black and green lines correspond to ICCF and CCCD, respectively, and the blue dotted and orange dashed lines represent time-lag probability distributions of MICA and JAVELIN, respectively. The vertical dashed lines represent a time lag of 0 days.

broad components of Balmer lines ($H\alpha$, $H\beta$ and $H\gamma$) and Helium lines (He I and He II); (5) moreover, narrow components from the Balmer and Helium lines, and some narrow forbidden lines (see details in Feng et al. (2021a)) are depicted by a series of single-Gaussian functions. We compare the widths of [O III] λ 5007 on the mean spectrum and the high-resolution spectrum from HST to estimate the instrumental broadening, which is about 1200 km s^{-1} . Moreover, the host galaxy and Fe II in the spectrum are weak and degenerate so that it is not easy to fit the host, therefore we limit the host's FWHM within 1100 and 1300 km s^{-1} . In the fitting, the widths and shifts of all narrow emission lines are bound to [O III] λ 5007, while the flux ratios of [O III] λ 5007 to [O III] λ 4959 and [N II] λ 6583 to [N II] λ 6548 are set to 3 and 2.96, respectively. Correspondingly, we first obtain a series of parameters by fitting the mean spectrum, including the spectral index of power law, the FWHM and shift of Fe II, and the flux ratios of all narrow lines relative to [O III] λ 5007. And then these parameters are fixed to the fitting of each individual spectrum. Figure 2 shows the decomposition of the mean spectrum (left) and one example of fitting an individual spectrum (right). We also fit the spectrum with a slit width of $5''.05$, using the same spectral index and flux ratios of narrow lines as the other spectra.

Finally, the broad emission-line fluxes are measured for the relevant emission lines from the best-fit model to each individual spectrum, and are summarized in Table 1. The light-curve error actually contains both Poisson deviation and systematic uncertainty. The systematic errors are caused by the conditions of weather and telescope, which would lead to additional impact on our measurements. We follow Du et al. (2014) and apply the median smooth method to assess such errors. The light curves are displayed in the left panel of Figure 3. However, Fe II is too weak to accurately measure its variability and has not been taken to be analyzed in the present work.

3.2. Variability Characteristics

We utilize the following ways to describe the statistical characteristics of the data. The first is the sample mean flux, defined as

$$\langle F \rangle = \frac{1}{N} \sum_{i=0}^N F_i, \quad (1)$$

where F_i is i -th flux and N is the total number of observations. The second is the sample standard deviation, written as

$$S = \left(\frac{1}{N-1} \sum_{i=0}^N (F_i - \langle F \rangle)^2 \right)^{1/2}. \quad (2)$$

The third is the fractional variability amplitude F_{var} to describe AGN intrinsic variability (Rodríguez-Pascual et al. 1997),

$$F_{\text{var}} = \frac{(S^2 - \Delta^2)^{1/2}}{\langle F \rangle}, \quad (3)$$

where $\Delta^2 = \frac{1}{N} \sum_{i=0}^N \Delta_i^2$, and Δ_i is the uncertainty of F_i . According to Edelson et al. (2002), the error σ_{var} of F_{var} is expressed as

$$\sigma_{\text{var}} = \frac{1}{F_{\text{var}}} \left(\frac{1}{2N} \right)^{1/2} \frac{S^2}{\langle F \rangle^2}. \quad (4)$$

The last is R_{max} , the ratio between the maximum and the minimum of the light curve. The relevant measurements are listed in Table 2.

Table 2. Light Curve Statistics

Light Curve	Mean Flux	Standard Deviation	F_{var} (%)	R_{max}
H α	167.73	6.06	3.49 ± 0.42	1.23
H β	52.78	2.86	5.30 ± 0.62	1.28
H γ	22.48	1.55	6.39 ± 0.84	1.34
He I	8.98	1.00	10.95 ± 1.27	1.50
He II	12.95	2.92	20.12 ± 2.86	2.57

NOTE—The emission-line fluxes are in units of $10^{-13} \text{ erg s}^{-1} \text{ cm}^{-2}$.

3.3. Intercalibration

We only add the g band of ZTF into the B band of Lijiang as the continuum light curve to analyze time lag, considering that the r band data of ZTF in our monitoring period is few. Before merging the data, we confirm that the time lag between the g and B bands is less than one day. Owing to utilizing different apertures and different filters, the datasets need to be intercalibrated. Here, we calibrate multi-band data via PyCALI⁶, which fits light curve through the damped random walk process and uses multiplicative and additive factors to regulate these data into a common scale (Li et al. 2014). And the intercalibrated parameters are obtained based on the Bayesian framework of the diffusive nested sampling algorithm (Brewer et al. 2011). Finally, the calibrated data are presented in the panel (a) of Figure 3 as the continuum light curve used in subsequent analyses, and the data are given in Table 1.

In addition, we collect the historical light curves of NGC 4151 from previous literature to probe the long-term variations of NGC 4151, involving 5100 \AA continuum (Bentz et al. 2006; Shapovalova et al. 2008; De Rosa et al. 2018), B band (Lyu & Rieke 2021), b and v bands (Edelson et al. 2017), as well as sky survey data, like V and g bands of ASAS-SN, g and r bands of ZTF. Similarly, we also scale and shift these data with the B band of Lijiang through PyCALI (see Figure 4).

⁶ <https://github.com/LiyiAstroph/PyCALI>

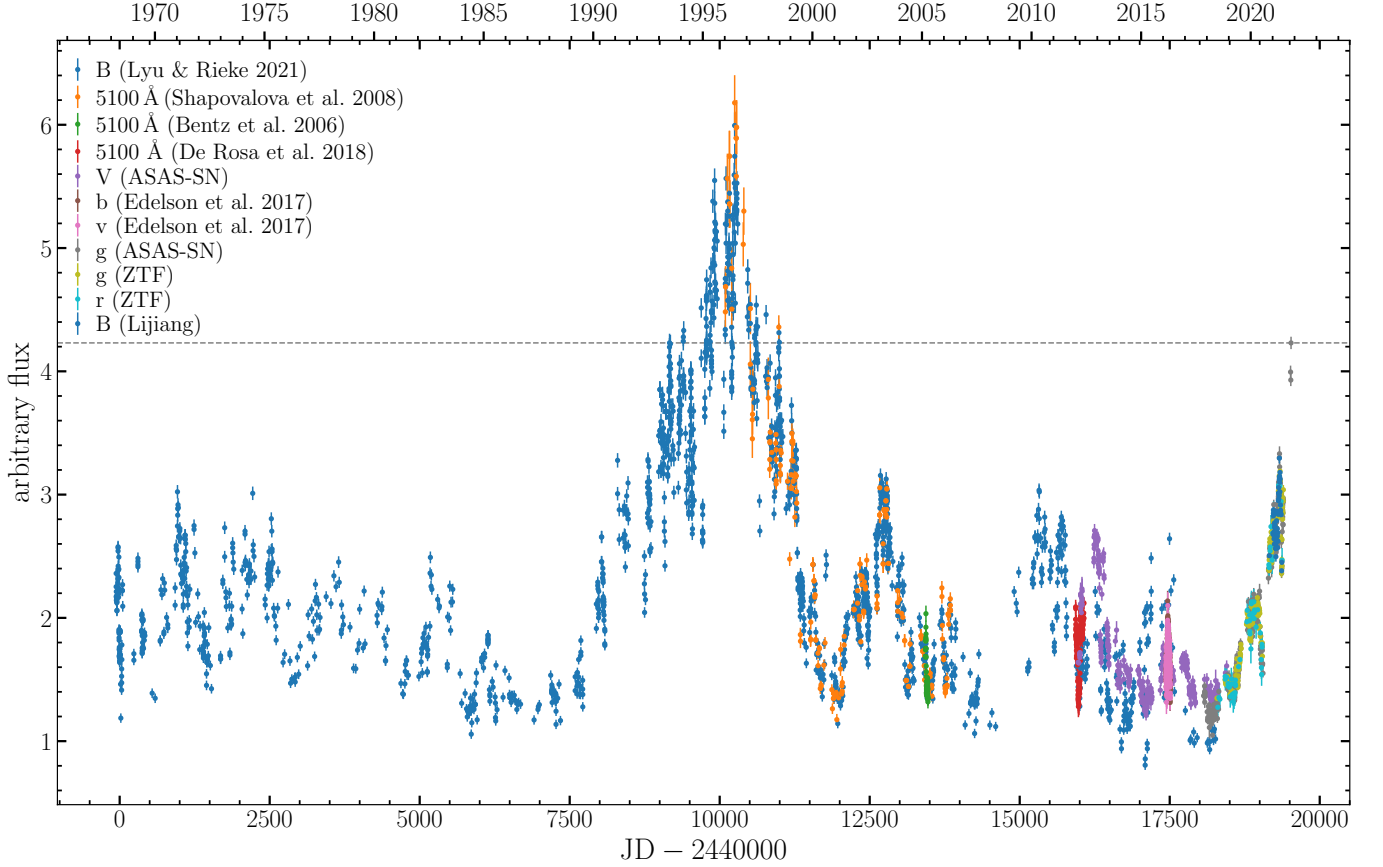


Figure 4. This is the long-term light curve of NGC 4151, which was generated by combing the collected continuum and photometry with the B band of Lijiang. The details about the intercalibrated data can be seen in Section 3.3. The horizontal dashed line represents the latest peak.

Table 3. Rest-frame Time Lags

Line	τ_{\max}	τ_{cent}	τ_{MICA}	τ_{JAV}	τ_{Mean}
H α	0.81	$5.00^{+0.84}_{-3.80}$	$9.28^{+2.91}_{-2.50}$	$8.60^{+1.80}_{-1.55}$	$7.63^{+1.85}_{-2.62}$
H β	0.88	$4.95^{+2.12}_{-1.20}$	$6.94^{+1.21}_{-1.27}$	$6.73^{+0.91}_{-0.91}$	$6.21^{+1.41}_{-1.13}$
H γ	0.81	$4.90^{+1.99}_{-2.61}$	$5.95^{+1.69}_{-1.88}$	$6.16^{+1.26}_{-1.33}$	$5.67^{+1.65}_{-1.94}$
He I	0.91	$1.46^{+0.86}_{-1.52}$	$1.52^{+1.02}_{-1.00}$	$1.78^{+0.70}_{-0.83}$	$1.59^{+0.86}_{-1.11}$
He II	0.90	$0.23^{+1.76}_{-1.39}$	$0.55^{+0.91}_{-0.94}$	$0.59^{+1.00}_{-0.84}$	$0.46^{+1.22}_{-1.06}$

NOTE— τ_{Mean} is the mean value of τ_{cent} , τ_{MICA} , and τ_{JAV} in units of days.

4. ANALYSIS AND RESULTS

4.1. Mean Time Lags

In order to investigate the responses of broad emission lines to continuum variations, we take the intercalibrated photometry light curve in Section 3.3 as the continuum light curve used to analyze time lags of emission lines with respect to the continuum variations. Three approaches are adopted to estimate time lags between emission lines and continuum, which include the interpolated cross-correlation function (ICCF; Gaskell & Sparke 1986; Gaskell & Peter-

son 1987), MICA⁷ (Li et al. 2016), and JAVELIN (Zu et al. 2011).

Traditionally, the ICCF is the most commonly used method for measuring time lags, and we choose the centroid of a region with the correction coefficients $r \geq 0.8r_{\max}$ as a time lag τ_{cent} , where r_{\max} is the maximum correlation coefficient. Similar to Peterson et al. (1998, 2004), we utilize the “flux randomization” (FR) and “random subset selection” (RSS) procedures to determine the lag uncertainties. Accordingly, a cross-correlation centroid distribution (CCCD) is built by 10^4 Monte Carlo realizations of the FR/RSS procedures, and we set the 15.87% and 84.13% quantiles of the CCCD as the lower and upper bounds of the lag.

MICA and JAVELIN are dependent on the damped random walk model, while the specific shapes of transfer functions are different. Specially, MICA and JAVELIN adopt the superposition of a set of moved Gaussian functions and a top-hat function as transfer function, respectively. For simplicity, we apply one Gaussian as the transfer function of MICA. The Gaussian and the top-hat centers stand for time delays in MICA and JAVELIN, respectively. Additionally, their time-lag posterior probability distributions are evaluated by

⁷ <https://github.com/LiyAstroph/MICA2>

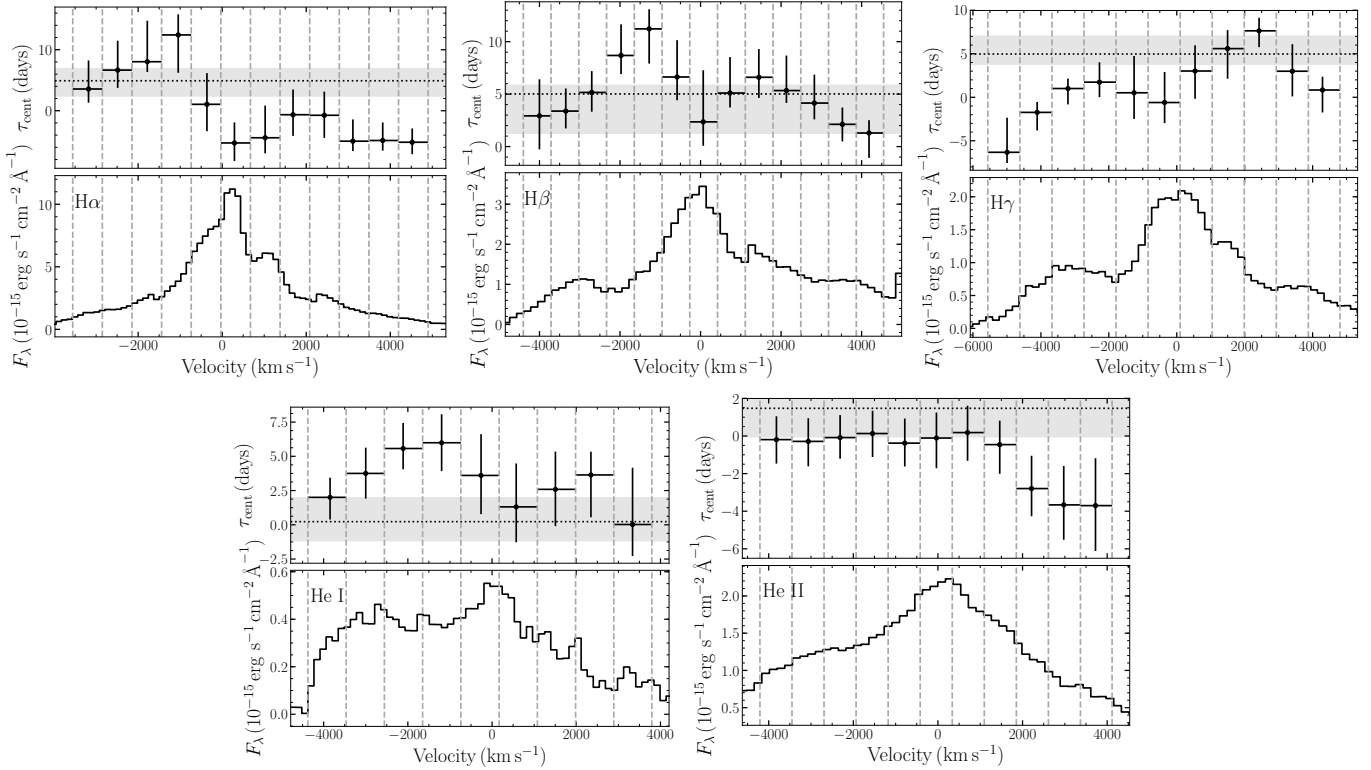


Figure 5. The velocity-resolved time-delay results of H α , H β , H γ , He I, and He II. The top panel in each subgraph shows the velocity-resolved structure for each emission line. In each panel, the horizontal dotted line and grey band represent the ICCF measured lag and CCD estimated errors, respectively. The vertical dashed lines denote the edges of each velocity bin. The bottom panel in each subgraph shows the rms spectrum of each emission line, for which the continuum is subtracted.

the Monte Carlo Markov Chain (MCMC) technique. The medians of their distributions are taken as time delays for MICA and JAVELIN, respectively. The lower and upper uncertainties of the time delays are determined by the 15.87%, and 84.13% quantiles of the relevant distributions. Besides that, both MICA and JAVELIN can reconstruct light curves, and the reconstructed results are filled with blue and orange blocks individually, as shown in the left panels of Figure 3.

The time lags calculated from these three ways are listed in Table 3, where τ_{MICA} and τ_{JAV} are the time lags measured by MICA and JAVELIN, respectively. Additionally, the time-lag posterior probability distributions are demonstrated in the right panels of Figure 3. Remarkably, the results of MICA and JAVELIN are consistent with each other, and are also in agreement with the ICCF measurements except H α and H β . Overall, the time lags measured by the ICCF method are lower than the results of the other two methods. This may be that both MICA and JAVELIN describe the light curve based on the damped random walk model, while ICCF directly linearly interpolates the light curve. Therefore, the measured lags will be affected by the principle difference between the ICCF and the MICA and JAVELIN, as well as some scattered points or gaps on the light curve, which may be why the ICCF lags are generally lower than the MICA and JAVELIN lags. We also find that time lags measured by each method follow $\tau_{\text{H}\alpha} > \tau_{\text{H}\beta} > \tau_{\text{H}\gamma} > \tau_{\text{He I}} > \tau_{\text{He II}}$, which are radial

stratification related to optical depths (Korista & Goad 2004) and ionization energy (Collin-Souffrin & Lasota 1988). We adopt the mean values of their respective three time lags in the subsequent analyses. We also compute the ratios of the mean lags of H α , H β , H γ , He I, and He II relative to H β to be 1.23 : 1.00 : 0.91 : 0.26 : 0.07.

4.2. Velocity-resolved Lags

The time lags between continuum and broad emission lines, measured in Section 4.1, characterize the mean sizes of the BLRs. By analyzing time series at different line-of-sight velocity bins, that is, velocity-resolved time lags, it is possible to yield some information about the kinematics and geometry of BLR. Note that the results of this approach are not necessarily accurate, as weak reverberation effects are ignored using the mean time lag for each bin (see De Rosa et al. 2018). There are three patterns to depict the kinematics of BLR, including virialized, inflowing, and outflowing motions. If lags at the line center are longer than those at line wings, the BLR is a virialized motion. When the lags of blueshifted velocity bins are longer than those of redshifted velocity bins, the BLR is an infall model, otherwise, it is the signature of outflow.

Below are the detailed steps for velocity-resolved RM. First, we select two windows on both sides of the emission line on the rms spectrum to fit the underlying continuum with

a straight line. Second, we divide each continuum-subtracted emission line into several velocity-space bins with an equal velocity interval. Then we apply these bins in individual spectrum to obtain their light curves, which are shown in the Appendix A. Finally, we perform ICCF between the light curves of emission line and continuum for each bin to measure lag with uncertainties estimated by CCCD. The velocity-dependent lags are shown in Figure 5. Indeed, we employ a different method from Section 3.1 to decompose emission lines, and this method used here can mitigate the degeneracy in the line wings introduced by the multi-component spectral fitting. Furthermore, the measurements from each method are generally consistent.

We note that velocity-delay structures of H α , H β , H γ , and He I are complicated. All the four emission lines show the double-peaked profiles of velocity-delay structures, but are not identical to each other. The blue-side peaks are larger than the red-side ones in H α , H β , and He I, but H γ appears to have a larger red-side peak. For H γ , it may be affected by [O III] λ 4363. Additionally, He II shows an infalling motion, however it seems unreliable. In the individual spectrum, He II is weak and blended with Fe II, making it hard to acquire a reliable velocity-delay structure. In short, since the velocity-resolved lags of H α , H β , and He I are consistent, we treat this kind of signature as the BLR kinematics, which may be a combined effect between virial and inflow motions. Mrk 6 also shows a similar velocity-delay structure (Doroshenko et al. 2012; Grier et al. 2013b; Du et al. 2018). However, in 2012 (De Rosa et al. 2018), the pattern of NGC 4151 is virialized motion, perhaps indicating a change in the kinematics of BLR. In addition, Bentz et al. (2022) reanalyzed RM data from NGC 4151 in 2005, and modeled these data to constrain the geometry and kinematics of BLR. The results indicate that the BLR can be characterized by a thick disk with opening angle $\sim 57^\circ$ and inclination angle $\sim 58^\circ$, and the kinematics of BLR are dominated by eccentric bound orbits, about 10% of the orbits tending to be near-circular motions. The above results further support that the kinematics of BLR have changed, as well as the geometry of BLR.

4.3. Black Hole Mass and Accretion Rate

Assuming that BLR clouds are bound by the gravity of the black hole and follow the virialized motion, the black hole mass can be expressed as

$$M_\bullet = f \frac{R_{\text{BLR}}(\Delta V)^2}{G} \equiv f M_{\text{vir}}, \quad (5)$$

where $R_{\text{BLR}} = c\tau$ represents the mean size of BLR, c is the speed of light, τ is the mean time lag of the BLR, G is the gravitational constant, ΔV is the broad emission-line velocity, usually characterized by the emission-line width, f is the virial factor, depending on geometry, kinematics, and inclination of the BLR, and M_{vir} is virial product.

The line width is generally depicted by FWHM or line dispersion σ_{line} of a mean or rms spectrum. σ_{line} is expressed as

$$\sigma_{\text{line}}^2(\lambda) = \frac{\int \lambda^2 F(\lambda) d\lambda}{\int F(\lambda) d\lambda} - \left[\frac{\int \lambda F(\lambda) d\lambda}{\int F(\lambda) d\lambda} \right]^2, \quad (6)$$

where $F(\lambda)$ is the flux density of emission-line profile at λ . Here, we present line-width measurements of a mean spectrum, and utilize the FWHM to estimate M_\bullet . Because the rms spectrum contains narrow line residuals and produces unreliable line widths, we do not use them here, but instead introduce them in Section 5.4.

We use the bootstrap technique to assess the line width and corresponding uncertainties. Specifically, we randomly select N spectra with replacement from N spectra, and then create a new mean spectrum after removing the repeated spectra. This process is repeated 1000 times to generate 1000 new mean spectra. Regarding each new mean spectrum, we adopt the spectral decomposition method and employ the best-fitting model in Section 3.1 to fit it, thereby acquiring FWHMs of broad emission lines from the fitted Gaussian models. The FWHMs and errors of emission lines are calculated by the median and the standard deviation of these measurements. Then, we subtract the fitting models except for broad emission-line components from the aforementioned mean spectra, and this subtraction generates the corresponding residual spectra. The distribution of σ_{line} is measured from the residual spectra for each broad emission line. The median and the standard deviation of this distribution are regarded as the measured values of σ_{line} and its error, respectively. The above FWHM and σ_{line} also need to subtract instrumental broadening contribution in quadrature, which is about 1200 km s^{-1} measured in Section 3.1, and the corrected line widths are summarized in Table 4.

The f factor is estimated from the following methods: the black hole mass and stellar velocity dispersion ($M_\bullet - \sigma_*$) relation (e.g., Onken et al. 2004; Woo et al. 2010; Grier et al. 2013a; Ho & Kim 2014), the BLR dynamical modeling analysis in a single AGN (Pancoast et al. 2012; Li et al. 2013, 2018), the widths and shifts of redward shifted broad emission lines (Liu et al. 2017, 2022; Mediavilla et al. 2020), and fitting the spectral energy distributions with the accretion disk model (Mejía-Restrepo et al. 2018). Kormendy & Ho (2013) showed that $M_\bullet - \sigma_*$ relation is related to the bulge type, thus we adopt the f factor obtained from Ho & Kim (2014), who derived it by subdivided bulge types. Due to a classical bulge in NGC 4151 (Ho & Kim 2014), we utilize $f = 1.3$, τ_{mean} , and FWHM in the mean spectrum to measure M_\bullet , and also provide M_{vir} in Table 4. We note that the black hole masses measured by the different emission lines are consistent with each other within errors, though the masses estimated from the Balmer lines are larger than those from He I and He II.

The dimensionless accretion rate is defined as $\dot{M} = \dot{M}_\bullet c^2 / L_{\text{Edd}}$, where \dot{M}_\bullet is the mass accretion rate and L_{Edd} is the Eddington luminosity (Wang et al. 2014). Based on the

Table 4. Time Lags, Line Widths, and Black Hole Masses

Line	τ_{Mean}	τ_{Tot}	FWHM	σ_{line}	M_{vir}	M_{\bullet}	M'_{\bullet}
	(days)		(km s ⁻¹)		($\times 10^7 M_{\odot}$)		
H α	7.63 ^{+1.85} _{-2.62}	8.45 ^{+2.17} _{-2.96}	4897 \pm 5	2069 \pm 2	3.57 ^{+0.87} _{-1.23}	4.64 ^{+1.13} _{-1.59}	5.14 ^{+1.32} _{-1.80}
H β	6.21 ^{+1.41} _{-1.13}	7.03 ^{+1.73} _{-1.47}	5003 \pm 13	2074 \pm 5	3.03 ^{+0.69} _{-0.55}	3.94 ^{+0.90} _{-0.72}	4.47 ^{+1.10} _{-0.93}
H γ	5.67 ^{+1.64} _{-1.94}	6.50 ^{+1.96} _{-2.28}	4799 \pm 20	2011 \pm 8	2.55 ^{+0.74} _{-0.87}	3.31 ^{+0.96} _{-1.13}	3.80 ^{+1.15} _{-1.33}
He I	1.59 ^{+0.86} _{-1.11}	2.41 ^{+1.18} _{-1.45}	6031 \pm 50	2340 \pm 11	1.13 ^{+0.61} _{-0.79}	1.46 ^{+0.79} _{-1.03}	2.23 ^{+1.09} _{-1.34}
He II	0.46 ^{+1.22} _{-1.06}	1.28 ^{+1.54} _{-1.40}	7099 \pm 52	2375 \pm 6	0.45 ^{+1.20} _{-1.04}	0.58 ^{+1.56} _{-1.35}	1.64 ^{+1.97} _{-1.78}

NOTE— τ_{Mean} is the mean lag of three methods in Section 4.1, τ_{Tot} is the result of τ_{Mean} plus $\tau_{\text{b-uv}}$ (see details in Section 5.3). FWHM and σ_{line} represent line widths of mean spectrum. M_{vir} is the virial product, M_{\bullet} is the black hole mass when adopting $f = 1.3$ and not considering the error of f , and M'_{\bullet} is measurement with τ_{Tot} .

standard accretion disk model (Shakura & Sunyaev 1973), \dot{M} can be estimated by the following formula (Wang et al. 2014)

$$\dot{M} = 20.1 \left(\frac{\ell_{44}}{\cos i} \right)^{3/2} m_7^{-2}, \quad (7)$$

where $\ell_{44} = L_{5100}/10^{44} \text{erg s}^{-1}$, $m_7 = M_{\bullet}/10^7 M_{\odot}$, and i is the inclination of the accretion disk. Here, we adopt $i = 45 \pm 5^\circ$ that is the inclination of narrow-line region (NLR) in NGC 4151 (Das et al. 2005), which agrees with the inclination of the NLR bicone model reported by Fischer et al. (2013). Note that the inclination of NLR does not always coincide with accretion disk, BLR or torus. For instance, the inclination $i = 45^\circ$ disagrees with an average inclination of the accretion disk to be $\sim 20^\circ$ derived from Fe K α modeling (Nandra et al. 1997). From the fitting results of all individual spectra, we extract the AGN continuum component and obtain a mean flux of AGN continuum at 5100 Å, $29.95(\pm 5.99) \times 10^{-15} \text{erg s}^{-1} \text{cm}^{-2} \text{Å}^{-1}$, and then a luminosity of $L_{5100} = 4.56(\pm 0.91) \times 10^{42} \text{erg s}^{-1}$. Combining this luminosity with $M_{\bullet} = 3.94^{+0.90}_{-0.72} \times 10^7 M_{\odot}$ measured from H β , the value of \dot{M} is $0.02^{+0.01}_{-0.01}$ (not considering uncertainties of inclination), implying that NGC 4151 is a sub-Eddington accretor.

5. DISCUSSION

5.1. Long-term Variability Trend

We collect the historical light curves of NGC 4151 with a temporal baseline of ~ 53 years, and intercalibrate them in Section 3.3, as displayed in Figure 4. The light curve consists of a major outburst and a series of minor flares. And, some of these peaks and valleys are accompanied by different spectral types, i.e., multiple CL phenomena. For example, the spectral type of NGC 4151 is an intermediate type in Osterbrock & Koski (1976), but is close to type 2 in 1984 while the flux is also fading to a minimum (Penston & Perez 1984). When the flux reaches the maximum in 1996, the spectral type is Seyfert 1.5. The type changes to Seyfert 1.8 at the two minimum states in 2001 and 2005 (Shapovalova et al. 2008). Interestingly, during the period of 1996 – 1999, NGC 4151 has strong continuum, but the emission line flux is saturated and

does not respond to continuum variations (Shapovalova et al. 2008).

Previous optical RM programs (e.g., Bentz et al. 2006; De Rosa et al. 2018) are located around minima, while our RM campaign is situated on the rise and near the second outburst. Kaspi et al. (1996) made an RM campaign in 1993, when NGC 4151 is in the rising period of the first outburst. Section 5.5 will compare these RM results in details.

5.2. Changing kinematics of BLR

NGC 4151 has been monitored by several RM campaigns in the past, some of which provided velocity-resolved results that allowed us to study its BLR properties. The velocity-delay map for C IV $\lambda 1549$ was first measured in 1991, where the BLR structure of C IV is asymmetric. Also, the time lags are 2 days in the strong redshifted line wing, and less than 10 days in the weak blueshifted line wing, indicating that gas motion is infalling (Ulrich & Horne 1996). Additionally, Bentz et al. (2022) obtained the kinematics of BLR by modeling the RM data in 2005. And the motions of BLR are dominated by eccentric bound orbits, but 10% of orbits are near circular motions. In 2012, the BLR structure of H β was investigated, and the BLR was found to be in a virialized motion (De Rosa et al. 2018). However, when checking their result, we find that the redshifted velocity-bin lag is larger than the blueshifted velocity-bin lag at the same velocity, which reveals a signature of outflow. In this campaign, we measure multiple emission-line velocity-resolved delays, but virial and infall signatures coexist. In general, the kinematics of BLR have changed for unknown reasons, possibly suggesting an evolution of the BLR.

5.3. Influence of Time Lags between UV and B Bands

In 2016, a 69-day multi-band, covering X-ray, UV, and optical bands, monitoring campaign of NGC 4151 was carried out at *Swift* (Edelson et al. 2017). We note that the time delay between *uvw2* (with a central wavelength of 1928 Å) and *b* (with a central wavelength of 4395 Å) bands is $0.83^{+0.32}_{-0.34}$ days, denoted by $\tau_{\text{b-uv}}$. This value can be regarded as the size of radiation region of the *B* band, which should not be ignored in the analysis of lags between the BLR and ionization source. To date, there is no clear evidence that the size of the *B*/optical band can change significantly. Therefore,

we sum it with our measured τ_{Mean} and write it as τ_{Tot} after being corrected to the rest frame. Meanwhile, we employ τ_{Tot} , FWHM, and $f = 1.3$ to compute M_{\bullet} , denoted as M'_{\bullet} in Table 4.

The ratios of τ_{Tot} to τ_{Mean} increased by 0.108, 0.133, 0.146, 0.521, 1.815 in H α , H β , H γ , He I, and He II, respectively. Correspondingly, the black hole mass also has the same change. The UV/optical lag has a significant impact on the results of He I and He II, but a less impact on those of the Balmer lines. Moreover, considering the UV/optical lag would reduce the discrepancy in measuring the mass of the black hole using different emission lines.

5.4. Virial Test

In order to investigate the motion of BLR in NGC 4151, we should check whether it is governed by the gravity of the black hole and obeys the virial relation ($\Delta V \propto \tau^{-0.5}$). This can be achieved by the following test. First, we investigate this relation through our estimates of time lags and velocities. Regression analysis of $\Delta V \propto \tau^{\alpha}$ is run for τ_{Mean} and τ_{Tot} with FWHMs measured from the mean spectrum. The best fittings give slopes of $\alpha = -0.15 \pm 0.04$ and -0.21 ± 0.06 for the τ_{Mean} and τ_{Tot} data, respectively (see Figure 6). The two best-fit results deviate from that of the virial relation with $\alpha = -0.5$. It is evident that the slope of applying τ_{Tot} is closer to the virial relation but still deviates from it. This might be caused by too few data points. Therefore, we collected time lags and line widths from the UV emission-line measurements and other optical RM results. Our data and those collected data are listed in Table 5.

Considering that the lags of UV emission lines are not affected by accretion disk size because they are measured using UV continuum, we only add $\tau_{\text{b-uv}}$ to the lags of optical lines for analysis. However, most previous results only provide emission-line widths of the rms spectrum. In comparison with them, we also present σ_{line} of the rms spectrum. Similar to the way for the mean spectrum described in Section 4.3, the line widths and corresponding uncertainties are assessed using 1000 times bootstrapping rms spectrum. For an individual rms spectrum, the σ_{line} of each line is directly measured after subtracting the underlying continuum via a straight line. The straight line is fitted using two continuum windows on both sides of the emission line. The median and standard deviation of the σ_{line} distribution are taken as the final value of σ_{line} and associated error, respectively, while subtracting the instrumental broadening (see Table 5). However, it should be stressed that the narrow-line residuals also appear in the rms spectrum, which will cause uncertainty in the estimate of σ_{line} . We fit all the data of σ_{line} and time lag in Table 5, and obtain a slope of -0.36 ± 0.10 (see Figure 6), which is marginally consistent with the expected value of $\alpha = -0.5$ within the error bar. However, it should be noted that there is also sizable scatter. Additionally, the data points are basically distributed around the virial relation of $\Delta V \propto \tau^{-0.5}$, implying that the BLR of NGC 4151 is basically in a virialized motion.

Table 5. Rest-frame Lags, rms σ_{line} and Black Hole Masses

Method	Lag (day)	rms σ_{line} (km s $^{-1}$)	M_{\bullet} ^d ($\times 10^7 M_{\odot}$)	Reference
H α RM	7.63 $^{+1.85}_{-2.62}$	1772 \pm 59 ^b	2.94 $^{+0.74}_{-1.03}$	This work
H β RM	6.21 $^{+1.41}_{-1.13}$	2020 \pm 76 ^b	3.11 $^{+0.75}_{-0.61}$	This work
H γ RM	5.67 $^{+1.64}_{-1.94}$	2359 \pm 73 ^b	3.88 $^{+1.15}_{-1.35}$	This work
He I RM	1.59 $^{+0.86}_{-1.11}$	2004 \pm 48 ^b	0.78 $^{+0.43}_{-0.55}$	This work
He II RM	0.46 $^{+1.22}_{-1.06}$	3172 \pm 82 ^b	0.56 $^{+1.51}_{-1.31}$	This work
H α RM	11.00 $^{+4.10}_{-3.10}$	1721 \pm 47 ^b	4.01 $^{+1.51}_{-1.15}$	1, 3
H β RM	11.50 $^{+3.70}_{-3.70}$	1958 \pm 56 ^b	5.42 $^{+1.77}_{-1.77}$	1, 3
H α RM	3.20 $^{+1.90}_{-1.70}$	2422 \pm 79	2.31 $^{+1.38}_{-1.24}$	2, 3
H β RM	3.10 $^{+1.30}_{-1.30}$	1914 \pm 42	1.40 $^{+0.59}_{-0.59}$	2, 3
H β RM	6.57 $^{+1.12}_{-0.72}$	2680 \pm 64	5.80 $^{+1.03}_{-0.69}$	4
H β RM	6.59 $^{+0.19}_{-0.21}$	1940 \pm 22	3.05 $^{+0.11}_{-0.12}$	5
C IV RM	3.43 $^{+1.42}_{-1.24}$	5698 \pm 245	13.69 $^{+5.79}_{-5.09}$	6, 8
He II RM ^a	3.46 $^{+1.96}_{-1.60}$	5013 \pm 323	10.69 $^{+6.21}_{-5.13}$	6, 8
C III] RM	6.88 $^{+4.56}_{-3.82}$	2553 \pm 307	5.51 $^{+3.89}_{-3.34}$	6, 8
Mg II RM	6.81 $^{+1.73}_{-2.09}$	2581 \pm 179	5.58 $^{+1.61}_{-1.88}$	6, 8
C IV RM	3.27 $^{+0.83}_{-0.91}$	5140 \pm 113 ^c	10.62 $^{+2.74}_{-2.99}$	7, 8
He II RM ^a	2.59 $^{+1.10}_{-1.21}$	4530 \pm 92	6.54 $^{+2.79}_{-3.06}$	7, 8
C III] RM	3.44 $^{+1.51}_{-1.22}$	2817 \pm 81	3.36 $^{+1.49}_{-1.21}$	7, 8
Mg II RM	5.33 $^{+1.86}_{-1.76}$	2721 \pm 141	4.85 $^{+1.77}_{-1.68}$	7, 8
Gas dynamics	—	—	3.6 $^{+0.9}_{-2.6}$	9, 11
Stellar dynamics	—	—	4.27 $^{+1.31}_{-1.31}$	10, 11
Stellar dynamics	—	—	0.25 – 3.0	11
RM modeling	—	—	1.66 $^{+0.48}_{-0.34}$	12

NOTE—References: (1) Maoz et al. (1991), (2) Kaspi et al. (1996), (3) Peterson et al. (2004), (4) Bentz et al. (2006), (5) De Rosa et al. (2018), (6) Clavel et al. (1990), (7) Ulrich & Horne (1996), (8) Metzroth et al. (2006), (9) Hicks & Malkan (2008), (10) Onken et al. (2014), (11) Roberts et al. (2021), (12) Bentz et al. (2022).

^a Here He II refers to the He II λ 1640 line.

^b The value is uncertain, since the rms spectrum incorporate the narrow line residuals, and bring unconvinced line width measurements.

^c The value is also unsure, because that C IV line is strongly self-absorbed.

^d The values of M_{\bullet} measured by RM are corrected by $f = 6.3$, which is much larger than $f = 1.3$ because $f = 6.3$ corresponds to σ_{line} rather than FWHM.

5.5. Comparison with Previous Results

We mainly compare our measurements of broad-line lags and black hole mass of NGC 4151 with other published results. Historically, multiple RM campaigns for NGC 4151 had been carried out, and had measured the relevant time lags of optical and/or UV emission lines. Here, we separately introduce their results. In the RM monitoring of 1988, the time lag was 9 ± 2 days in both H α and H β (Maoz et al. 1991). Kaspi et al. (1996) measured time lags of 0–3 days for H α and H β with respect to continuum variations in 1993. Later, the above two data sets are reanalyzed by Peterson et al. (2004). Then, Bentz et al. (2006) and De Rosa et al. (2018) performed well-sampled RM campaigns in 2005 and 2012, respectively, and obtained $6.57^{+1.12}_{-0.76}$ and $6.59^{+0.19}_{-0.21}$ days of H β lags at the rest frame. In our work, the time lags of H α and H β are basically consistent with the above results of others. Additionally, Clavel et al. (1990) and Ulrich & Horne (1996) performed UV RM programs. Metzroth et al.

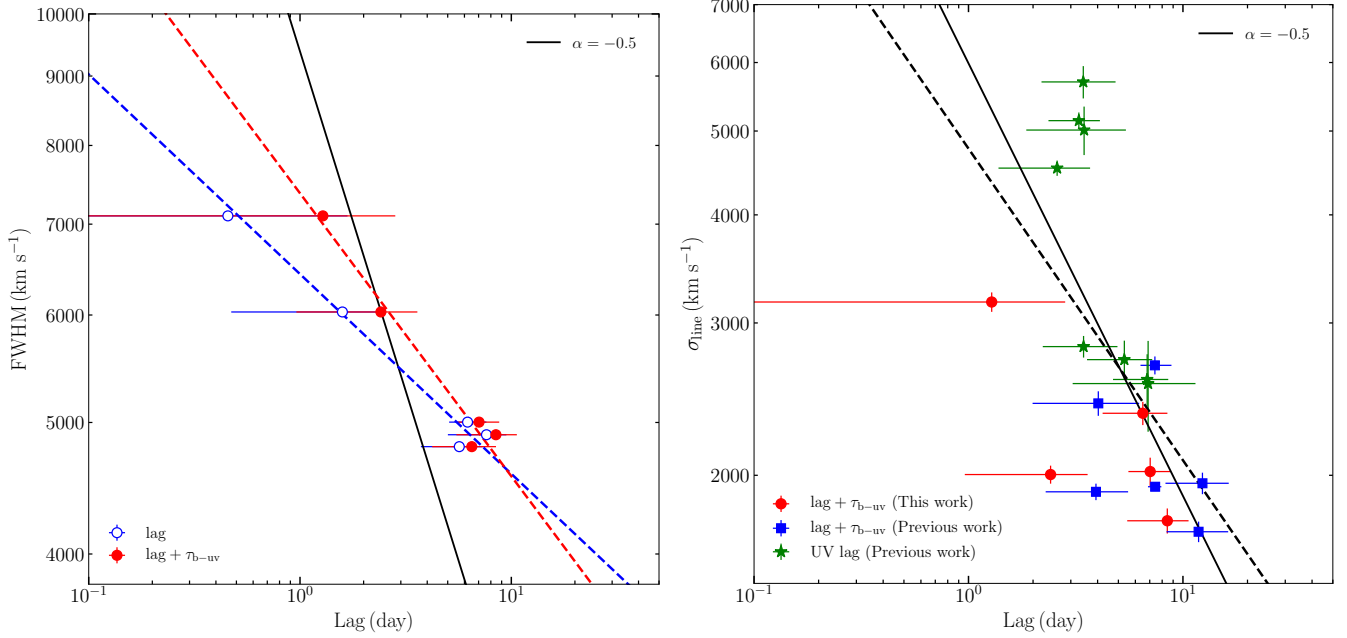


Figure 6. Line width vs. time lag. The left panel: our observational results of FWHM vs. time lag. The blue data is τ_{Mean} , and the red data is τ_{Mean} plus $\tau_{\text{b-uv}}$. The blue and red dashed lines represent the best fit lines with slopes of -0.15 ± 0.04 and -0.21 ± 0.06 , respectively. The right panel: rms σ_{line} vs. time lag for all the data. The black dashed line represents the best fit line with a slope of -0.36 ± 0.10 . The black solid line in each panel is the best fit line using the virial relation with a slope of -0.5 .

(2006) reanalyzed their data and obtained the corresponding lags and line widths.

On the other hand, the black hole mass of NGC 4151 has been measured by different methods, for instance, the gas dynamical modeling (Hicks & Malkan 2008), the stellar dynamical modeling (Onken et al. 2014; Roberts et al. 2021), the RM method (Peterson et al. 2004; Bentz et al. 2006; Metzroth et al. 2006; De Rosa et al. 2018), and the RM data modeling (Bentz et al. 2022). Thus, we can compare these measurements to check the reliability of different methods. The black hole masses measured by these methods are listed in Table 5. Here, the dynamical modeling results were unified by Roberts et al. (2021) according to the Cepheid distance of 15.8 ± 0.4 Mpc (Yuan et al. 2020). Because the virial coefficients used in different RM projects are different, we adopt $f = 6.3$ in Ho & Kim (2014) to adjust the RM results. Additionally, for consistency, we also give the values of M_{\bullet} estimated with rms σ_{line} measured in Section 5.4 (see Table 5). It's worth noting that the black hole masses determined by different methods are consistent within errors. However, the results for the UV lines are overall larger than others, even an order of magnitude.

6. CONCLUSION

Here, we report a new RM campaign on NGC 4151 and the detailed results are summarized below.

1. We measure time delays between multiple broad emission lines and continuum simultaneously, to be $7.63^{+1.85}_{-2.62}$, $6.21^{+1.41}_{-1.13}$, $5.67^{+1.65}_{-1.94}$, $1.59^{+0.86}_{-1.11}$, and $0.46^{+1.22}_{-1.06}$ days for the broad H α , H β , H γ , He I, and

He II lines, respectively. These lags satisfy $\tau_{\text{H}\alpha} > \tau_{\text{H}\beta} > \tau_{\text{H}\gamma} > \tau_{\text{He I}} > \tau_{\text{He II}}$, which are radial stratification and may be affected by optical depths and ionization energy. Besides that, the time lag ratios of H α , H β , H γ , He I, and He II relative to H β are $1.23 : 1.00 : 0.91 : 0.26 : 0.07$. If considering the time lag of the optical band relative to the UV band, it would bring more variation in the time lags of He I and He II.

2. It's the first time for NGC 4151 to explore velocity-resolved time lags of multiple optical emission lines. The velocity-resolved structures of H α , H β , and He I are consistent with each other, the lags of the blue wing are overall larger than those of the red wing, and the lags of the line core are larger than those of both wings, indicating that virial and infalling motions coexist. H γ may be affected by [O III] $\lambda 4363$, and He II is weak and likely contaminated by Fe II, causing less reliable results for H γ and He II. In comparison with previous velocity-resolved structures, we note that the kinematics of the BLR changes from inflow to virialization with outflow, and then to virial and inflow coexistence signature, indicating the evolutionary kinematics of the BLR.
3. Combining our measurements and the collected RM results including time delays and velocities, we verify that all the observational data of time lag and velocity for NGC 4151 basically follows a virial relation of $\Delta V \propto \tau^{-0.5}$.

4. We measure the black hole mass of NGC 4151 based on the FWHM of the mean spectrum, the time lag and $f = 1.3$, and the value is $3.94_{-0.72}^{+0.90} \times 10^7 M_{\odot}$ for $H\beta$. Furthermore, comparing our measurements with previous results, we find that they are consistent within errors. Using the black hole mass measured by $H\beta$, we calculate the dimensionless accretion rate to be $0.02_{-0.01}^{+0.01}$, indicating NGC 4151 is in a sub-Eddington accretion state.

NGC 4151 is one of the best-studied AGNs with multiple RM observations. Our result of the time lag of $H\beta$ is consistent with De Rosa et al. (2018), but the velocity-resolved results are quite different, which hints the evolution of kinematics of the BLR. This campaign of NGC 4151 is located at the rising phase of the second outburst, and it is worth continuously monitoring NGC 4151 to explore the origin of variable kinematics.

We thank the referee for useful comments that improved the manuscript. We are grateful to Zi-Xu Yang, Jun-Rong Liu, and Zhu-Heng Yao for their time and effort in our obser-

ations. This work is supported by the National Key R&D Program of China with No. 2021YFA1600404, the National Natural Science Foundation of China (NSFC; grants No. 11991051, 12103041, 12073068), the joint fund of Astronomy of the NSFC and the CAS (grant No. U1931131), and the science research grants from the China Manned Space Project with NO. CMS-CSST-2021-A06.

We acknowledge the support of the staff of the Lijiang 2.4m telescope. Funding for the telescope has been provided by Chinese Academy of Sciences and the People's Government of Yunnan Province. The Zwicky Transient Facility Collaboration is supported by U.S. National Science Foundation through the Mid-Scale Innovations Program (MSIP). This research has made use of the NASA/IPAC Extragalactic Database (NED) which is operated by the Jet Propulsion Laboratory, California Institute of Technology, under contract with the National Aeronautics and Space.

Facilities: Lijiang: 2.4 m

Software: IRAF (Tody 1986), DASpec (<https://github.com/PuDu-Astro/DASpec>), PyCALI (Li et al. 2014), MICA (Li et al. 2016), JAVELIN (Zu et al. 2011)

APPENDIX

A. VELOCITY-RESOLVED LIGHT CURVES

Here are velocity-space bin light curves and cross-correlation results for $H\alpha$, $H\beta$, $H\gamma$, He I, and He II, illustrated in Figure 7, 8 and 9.

REFERENCES

- Antonucci, R. 1993, ARA&A, 31, 473
- Barth, A. J., Bennert, V. N., Canalizo, G., et al. 2015, ApJS, 217, 26
- Barth, A. J., Pancoast, A., Bennert, V. N., et al. 2013, ApJ, 769, 128
- Bao, D.-W., Brotherton, M. S., Du, P., et al. 2022, arXiv:2207.00297
- Bellm, E. C., Kulkarni, S. R., Graham, M. J., et al. 2019, PASP, 131, 018002
- Bentz, M. C., Denney, K. D., Cackett, E. M., et al. 2006, ApJ, 651, 775
- Bentz, M. C., Walsh, J. L., Barth, A. J., et al. 2009, ApJ, 705, 199
- Bentz, M. C., Williams, P. R., & Treu, T. 2022, arXiv:2206.03513
- Blandford, R. D., & McKee, C. F. 1982, ApJ, 255, 419
- Boroson, T. A., & Green, R. F. 1992, ApJS, 80, 109
- Brewer, B. J., Páatay, L. B., & Csányi, G. 2011, Stat. Comput., 21, 649
- Bruzual, G. & Charlot, S. 2003, MNRAS, 344, 1000
- Brotherton, M. S., Du, P., Xiao, M., et al. 2020, ApJ, 905, 77
- Cackett, E. M., Bentz, M. C., & Kara, E. 2021, iScience, 24, 102557
- Cackett, E. M., Gelbord, J., Li, Y.-R., et al. 2020, ApJ, 896, 1
- Cardelli, J. A., Clayton, G. C., & Mathis, J. S. 1989, ApJ, 345, 245
- Clavel, J., Boksenberg, A., Bromage, G. E., et al. 1990, MNRAS, 246, 668
- Collin-Souffrin, S. & Lasota, J.-P. 1988, PASP, 100, 1041
- Das, V., Crenshaw, D. M., Hutchings, J. B., et al. 2005, AJ, 130, 945
- De Rosa, G., Fausnaugh, M. M., Grier, C. J., et al. 2018, ApJ, 866, 133
- Denney, K. D., Peterson, B. M., Pogge, R. W., et al. 2010, ApJ, 721, 715
- Du, P., Brotherton, M. S., Wang, K., et al. 2018, ApJ, 869, 142
- Du, P., Hu, C., Lu, K.-X., et al. 2014, ApJ, 782, 45
- Du, P., Lu, K.-X., Hu, C., et al. 2016, ApJ, 820, 27
- Doroshenko, V. T., Sergeev, S. G., Klimanov, S. A., et al. 2012, MNRAS, 426, 416
- Edelson, R. A., Alexander, T., Crenshaw, D. M., et al. 1996, ApJ, 470, 364
- Edelson, R., Gelbord, J., Cackett, E., et al. 2017, ApJ, 840, 41
- Edelson, R., Turner, T. J., Pounds, K. et al. 2002, ApJ, 568, 610

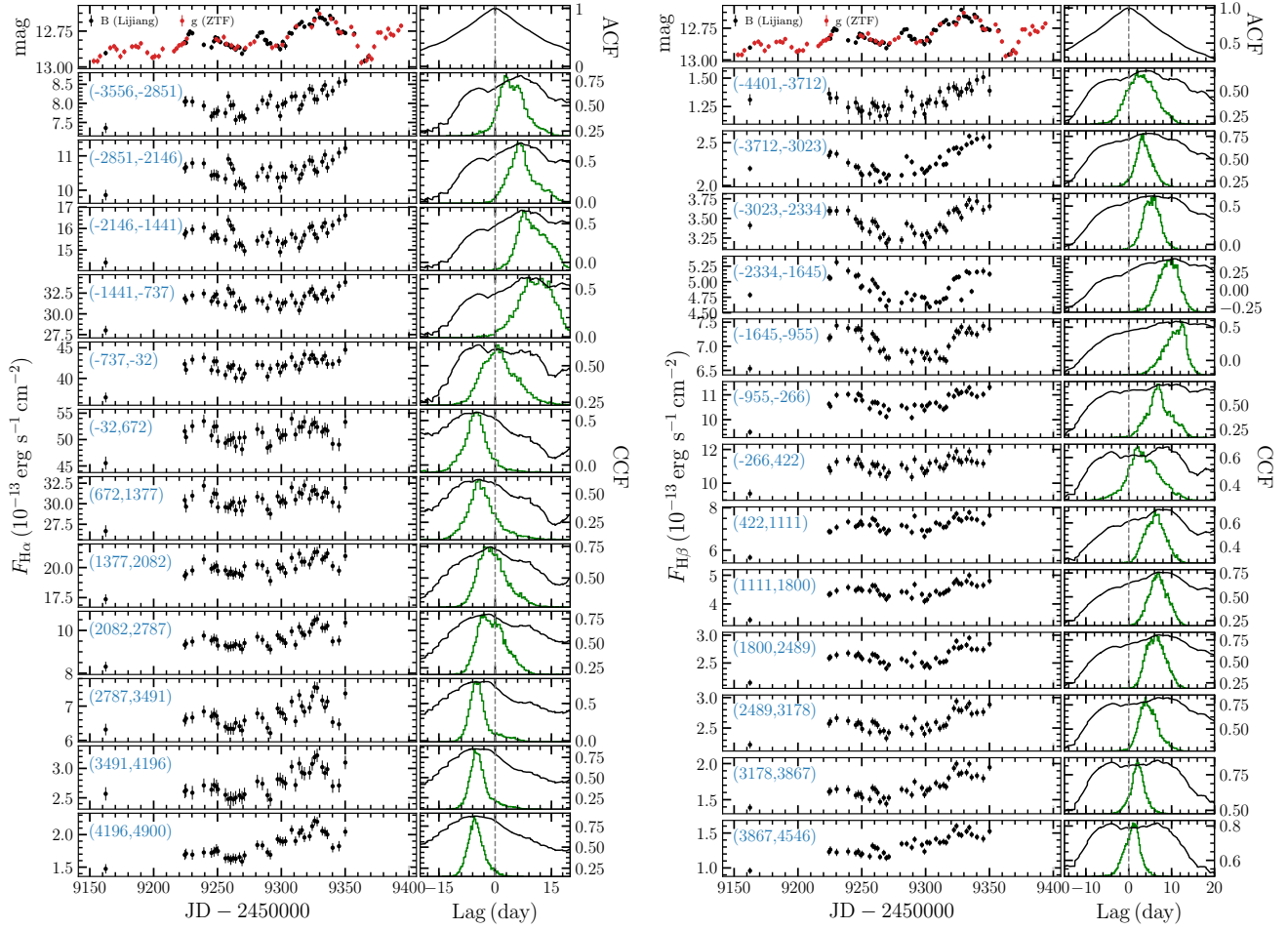


Figure 7. The $H\alpha$ (left) and $H\beta$ (right) results. The left panels are photometric and each bin light curves, where the photometry is g (ZTF) merged with B (Lijiang) results. The right panels display ACF of photometry, the cross-correlation results between each bin and photometry, including the ICCFs (black) and CCCDs (green).

Fausnaugh, M. M., Grier, C. J., Bentz, M. C., et al. 2017, *ApJ*, 840, 97
 Feng, H.-C., Hu, C., Li, S.-S., et al. 2021a, *ApJ*, 909, 18
 Feng, H.-C., Liu, H. T., Bai, J. M., et al. 2021b, *ApJ*, 912, 92
 Fian, C., Chelouche, D., Kaspi, S., et al. 2022, *A&A*, 659, A13
 Fischer, T. C., Crenshaw, D. M., Kraemer, S. B., et al. 2013, *ApJS*, 209, 1
 Förster, F., Cabrera-Vives, G., Castillo-Navarrete, E., et al. 2021, *AJ*, 161, 242
 Gaskell, C. M., & Peterson, B. M. 1987, *ApJS*, 65, 1
 Gaskell, C. M. & Sparke, L. S. 1986, *ApJ*, 305, 175
 Graham, M. J., Kulkarni, S. R., Bellm, E. C., et al. 2019, *PASP*, 131, 078001
 Gravity Collaboration, Sturm, E., Dexter, J., et al. 2018, *Nature*, 563, 657
 Grier, C. J., Martini, P., Watson, L. C., et al. 2013a, *ApJ*, 773, 90
 Grier, C. J., Peterson, B. M., Horne, K., et al. 2013b, *ApJ*, 764, 47
 Hicks, E. K. S. & Malkan, M. A. 2008, *ApJS*, 174, 31

Ho, L. C. & Kim, M. 2014, *ApJ*, 789, 17
 Horne, K., De Rosa, G., Peterson, B. M., et al. 2021, *ApJ*, 907, 76
 Hu, C., Du, P., Lu, K.-X., et al. 2015, *ApJ*, 804, 138
 Hu, C., Li, S.-S., Guo, W.-J., et al. 2020a, *ApJ*, 905, 75
 Hu, C., Li, Y.-R., Du, P., et al. 2020, *ApJ*, 890, 71
 Hu, C., Li, S.-S., Yang, S., et al. 2021, *ApJS*, 253, 20
 Kaspi, S., Maoz, D., Netzer, H., et al. 1996, *ApJ*, 470, 336
 Kaspi, S., Smith, P. S., Netzer, H., et al. 2000, *ApJ*, 533, 631
 Kochanek, C. S., Shappee, B. J., Stanek, K. Z., et al. 2017, *PASP*, 129, 104502
 Korista, K. T. & Goad, M. R. 2004, *ApJ*, 606, 749
 Kormendy, J. & Ho, L. C. 2013, *ARA&A*, 51, 511
 Koshida, S., Minezaki, T., Yoshii, Y., et al. 2014, *ApJ*, 788, 159
 Li, S.-S., Yang, S., Yang, Z.-X., et al. 2021, *ApJ*, 920, 9
 Li, Y.-R., Songsheng, Y.-Y., Qiu, J., et al. 2018, *ApJ*, 869, 137
 Li, Y.-R., Wang, J.-M., & Bai, J.-M. 2016, *ApJ*, 831, 206
 Li, Y.-R., Wang, J.-M., Ho, L. C., et al. 2013, *ApJ*, 779, 110
 Li, Y.-R., Wang, J.-M., Hu, C., et al. 2014, *ApJL*, 786, L6

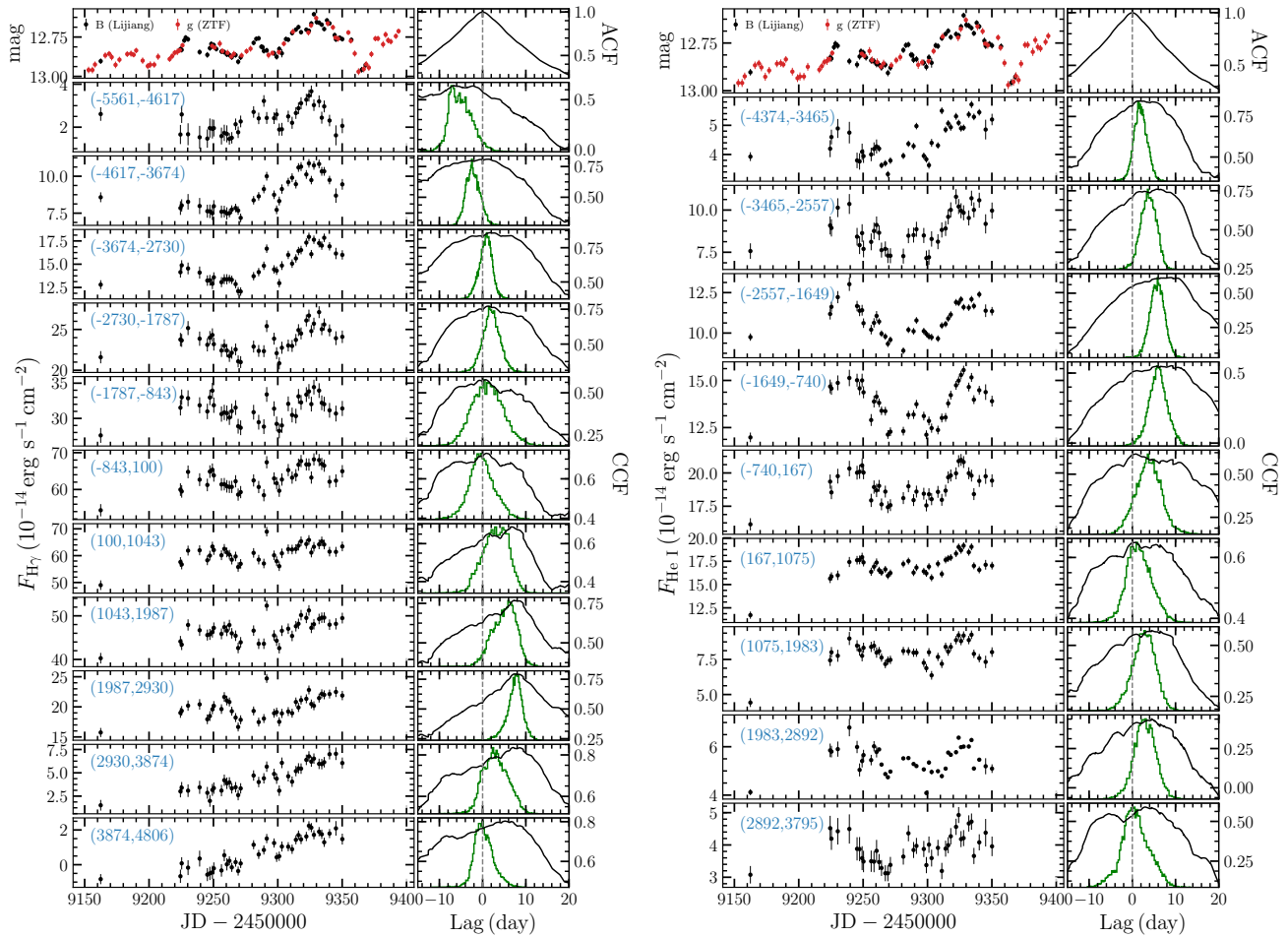


Figure 8. Same as Figure 7 but for the H γ (left) and He I (right) results.

Liu, H. T., Feng, H. C., & Bai, J. M. 2017, *MNRAS*, 466, 3323
 Liu, H. T., Feng, H. C., Li, S.-S., & Bai, J. M. 2022, *ApJ*, 928, 60
 Lu, K.-X., Bai, J.-M., Zhang, Z.-X., et al. 2019, *ApJ*, 887, 135
 Lu, K.-X., Wang, J.-G., Zhang, Z.-X., et al. 2021, *ApJ*, 918, 50
 Lyu, B., Wu, Q., Yan, Z., et al. 2022, *ApJ*, 927, 227
 Lyu, J. & Rieke, G. H. 2021, *ApJ*, 912, 126
 Maoz, D., Netzer, H., Leibowitz, E., et al. 1990, *ApJ*, 351, 75
 Maoz, D., Netzer, H., Mazeh, T., et al. 1991, *ApJ*, 367, 493
 Masci, F. J., Laher, R. R., Rusholme, B., et al. 2019, *PASP*, 131, 018003
 Mediavilla, E., Jiménez-vicente, J., Mejía-restrepo, J., et al. 2020, *ApJ*, 895, 111
 Mejía-Restrepo, J. E., Lira, P., Netzer, H., et al. 2018, *Nature Astronomy*, 2, 63
 Metzroth, K. G., Onken, C. A., & Peterson, B. M. 2006, *ApJ*, 647, 901
 Nandra, K., George, I. M., Mushotzky, R. F., et al. 1997, *ApJ*, 477, 602
 O'Donnell, J. E. 1994, *ApJ*, 422, 158

Oknyansky, V. L., Metlova, N. V., Taranova, O. G., et al. 2014, *Odessa Astronomical Publications*, 27, 47
 Onken, C. A., Ferrarese, L., Merritt, D., et al. 2004, *ApJ*, 615, 645
 Onken, C. A., Valluri, M., Brown, J. S., et al. 2014, *ApJ*, 791, 37
 Osterbrock, D. E. & Koski, A. T. 1976, *MNRAS*, 176, 61P
 Pancoast, A., Brewer, B. J., Treu, T., et al. 2012, *ApJ*, 754, 49
 Penston, M. V. & Perez, E. 1984, *MNRAS*, 211, 33P
 Peterson, B. M., Ferrarese, L., Gilbert, K. M., et al. 2004, *ApJ*, 613, 682
 Peterson, B. M., Wanders, I., Horne, K., et al. 1998, *PASP*, 110, 660
 Roberts, C. A., Bentz, M. C., Vasiliev, E., et al. 2021, *ApJ*, 916, 25
 Rodríguez-Pascual, P. M., Alloin, D., Clavel, J., et al. 1997, *ApJS*, 110, 9
 Sánchez-Sáez, P., Reyes, I., Valenzuela, C., et al. 2021, *AJ*, 161, 141
 Schlafly, E. F. & Finkbeiner, D. P. 2011, *ApJ*, 737, 103
 Shakura, N. I. & Sunyaev, R. 1973, *A&A*, 24, 337
 Shapovalova, A. I., Popović, L. Č., Collin, S., et al. 2008, *A&A*, 486, 99

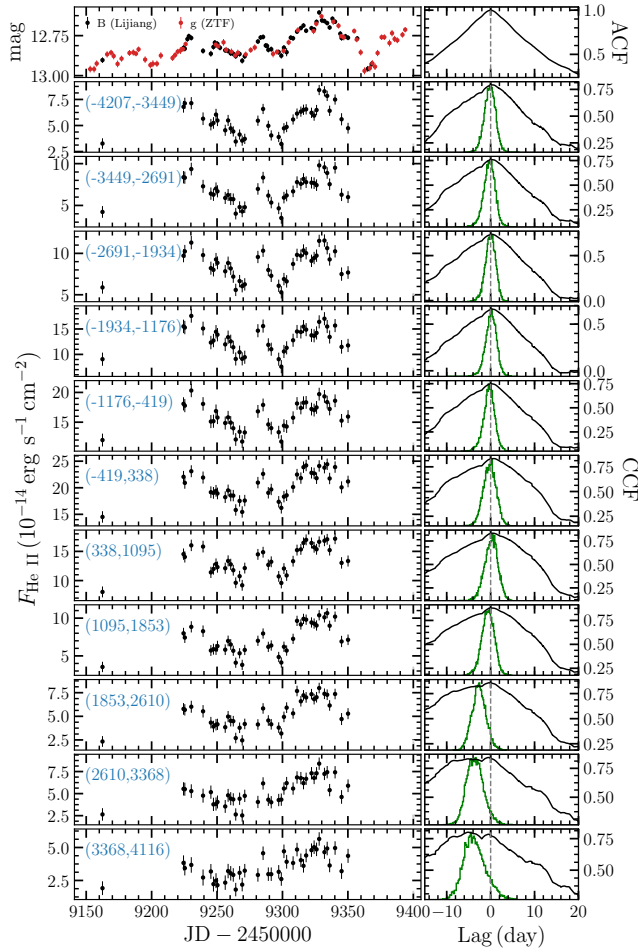


Figure 9. Same as Figure 7 but for the He II results.

Shappee, B. J., Prieto, J. L., Grupe, D., et al. 2014, *ApJ*, 788, 48
 Seyfert, C. K. 1943, *ApJ*, 97, 28
 Tody, D. 1986, *Proc. SPIE*, 627, 733
 U, V., Barth, A. J., Vogler, H. A., et al. 2022, *ApJ*, 925, 52
 Ulrich, M.-H. & Horne, K. 1996, *MNRAS*, 283, 748
 Villafaña, L., Williams, P. R., Treu, T., et al. 2022, *ApJ*, 930, 52
 Wang, C.-J., Bai, J.-M., Fan, Y.-F., et al. 2019, *RAA*, 19, 149
 Wang, J.-M., Du, P., Hu, C., et al. 2014, *ApJ*, 793, 108
 Williams, P. R., Pancoast, A., Treu, T., et al. 2018, *ApJ*, 866, 75

Woo, J.-H., Treu, T., Barth, A. J., et al. 2010, *ApJ*, 716, 269
 Xiao, M., Du, P., Lu, K.-K., et al. 2018, *ApJL*, 865, L8
 Xin, Y.-X., Bai, J.-M., Lun, B.-L., et al. 2020, *RAA*, 20, 149
 Yuan, W., Fausnaugh, M. M., Hoffmann, S. L., et al. 2020, *ApJ*, 902, 26
 Zhang, Z.-X., Du, P., Smith, P. S., et al. 2019, *ApJ*, 876, 49
 Zu, Y., Kochanek, C. S., & Peterson, B. M., 2011, *ApJ*, 735, 80